Rapid Communications

# Onset of the magnetized arc and its effect on the momentum of a low-power two-stage pulsed magneto-plasma-dynamic thruster

D. B. Zolotukhin,[1,2,*] K. P. Daniels,[1] L. Brieda,[3] and M. Keidar[1]

[1]*The George Washington University, 800 22nd Street, Northwest, Washington, DC 20052, USA*

[2]*Tomsk State University of Control Systems and Radioelectronics, 40 Lenin Avenue, Tomsk 634050, Russia*

[3]*Particle In Cell Consulting LLC, Westlake Village, California 91362, USA*

(Received 5 May 2020; accepted 14 July 2020; published 17 August 2020)

A new type of plasma accelerator—a low-power (<30 W), miniature (cm-sized), two-stage pulsed magneto-plasma-dynamic thruster—has been proposed. Being magnetized by an axially symmetric dc magnetic field of ∼200 mT, the vacuum arc discharge demonstrates a threshold behavior: Parameters such as thrust and the thrust-to-power ratio rapidly jump after a certain dc voltage (∼30 V) is applied on the accelerating electrode. We show that such an effect improves the thrust (from ∼2 to ∼210 μN), efficiency (from ∼1% to 50%), and thrust-to-power ratio (from ∼0.5 to ∼18 μN/W).

DOI: 10.1103/PhysRevE.102.021203

Magneto-plasma-dynamic (MPD) thrusters are typically powerful (with an average power within the range of kW to hundreds of kW), high-thrust propulsion engines with an electromagnetic Lorentz force $J \times B$ that accelerates and expels plasma and creates thrust [1]. Physical effects and plasma instabilities in MPD and Hall thrusters have been actively studied [2,3]. MPD thrusters have a high thrust density and do not require an ion-absorbing grid system, dangerously high voltages, and lifetime-limited cathode neutralizers. In applied-field MPD thrusters that use an external coil to create a magnetic field, the Lorentz force is generated mainly as a result of the vector product of a large current $J$ flowing in the azimuthal direction in the plasma and radial component $B_r$ of the magnetic field of the coil. However, until now, applied-field MPD thrusters were able to achieve high efficiency (around 70%) only at high-power levels (∼20 kW) [1,4]. The fast-growing popularity of small satellites for low Earth orbit and even interplanetary space missions [5,6] requires the development of new types of efficient, miniature, lightweight, reliable, and low-power propulsion systems [7,8]. This makes promising the ambitious idea to scale down in power and size the applied-field MPD thruster to fit inside a small satellite. With such scaling, the immediate problem of satisfying conflicting requirements arises—there is a need to provide a thruster with a relatively high thrust (up to mN), high efficiency, and high thrust-to-power ratio (∼tens of μN/W) simultaneously with small mass, dimensions, and low-power consumption. This challenge can be overcome by a two-stage pulsed (up to ms pulse length), cm-sized, low-power (1–30 W) MPD thruster, with the low-power (∼several W) first stage based on microcathode arc thrusters (μCATs) creating an almost fully ionized preliminary plasma [9,10] as a result of a triggerless vacuum arc between two solid-state (metallic) electrodes [8]. The preliminary plasma then initiates a more powerful (up to 30 W for an accelerating stage voltage of ∼60 V) arc discharge in an external magnetic field in the second stage, which creates the main accelerated plasma flow which can be throttled by varying the voltage on the accelerating electrode. Such a thruster configuration is similar to the more powerful and single-staged so-called pulsed metallic-plasma generators [11] or pulsed vacuum arc thrusters [12–14] that have been studied at least since the end of the 1960s. The operation of just one stage does not allow one to vary the thrust and specific impulse of the thruster, while the operation of two independently controlled stages allows one to flexibly control and choose the thruster operation regimes. In one regime, when just the first stage is arcing, the thruster has a low consumption of the cathode material (and consequently a high specific impulse), and this regime is suitable for the drag compensation or long-term acceleration of the satellite. Another regime, when both stages are firing, provides controllably high thrust values, and this regime is suitable for maneuvering and orbit change.

In this Rapid Communication, we report the interesting physical phenomena that appear in a two-stage μCAT-MPD thruster—parameters such as thrust, thrust-to-power ratio, and efficiency jump after a certain threshold voltage on the accelerating electrode, thereby allowing a drastic increase in the mentioned parameters by many tens of times.

Experiments were conducted with the μCAT-MPD thruster prototype described in Fig. 1. A single coaxial μCAT, with a central copper cathode and an outer annular copper anode, was used as the first stage (preliminary source of plasma). This plasma was expelled toward the opening of the accelerating MPD electrode with a positive dc bias $U_{\mathrm{MPD}}$ of up to 63 V. The thruster's first-stage face and accelerating electrode opening were placed in a field of an axially magnetized permanent ring magnet (with an inner diameter of 1.27 cm, outer diameter of 2.54 cm, and length of 1.27 cm) with an induction of ∼0.2 T on its axis [Fig. 1(a)]. The length of the thruster was 3.5 cm, and the diameter of the opening of the accelerating

*ZolotukhinDen@gmail.com

 

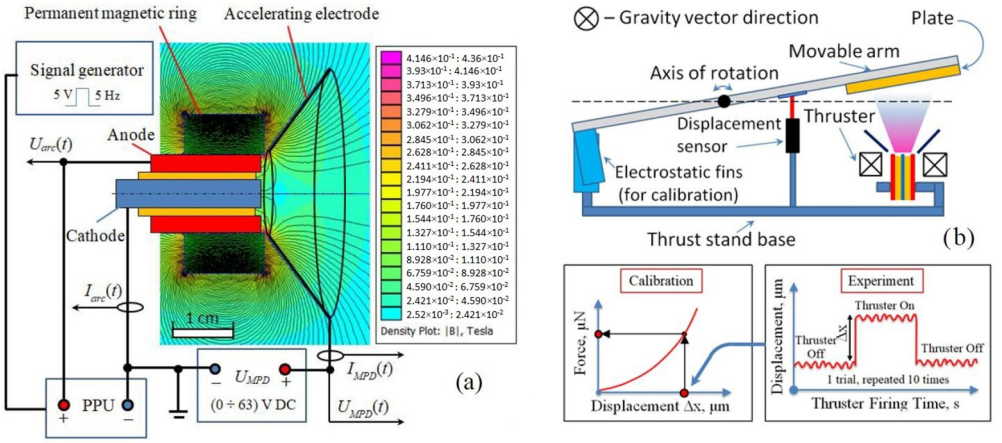


FIG. 1. (a) Schematic of MPD thruster and its circuitry, and (b) sketch of the indirect thrust measurements using the thrust stand.

MPD electrode was 4 cm. A large electron current $J$ toward the positively biased accelerating MPD electrode, as a result of the interaction between the radial component of magnetic field $B_r$, resulted in a Lorentz force $J \times B_r$, which in turn led to the acceleration of the plasma toward the accelerating electrode opening. Since $U_{\mathrm{MPD}}$ could be easily varied, the thrust gain was also controllable. For the first-stage power processing unit (PPU) we employed a well-known inductive storage pulsing circuit with a stored energy in a ferrite-core inductor of 550 μH and released it to the first stage of the thruster with a powerful insulated gate bipolar transistor (IGBT) gated by a rectangular-pulse signal generator with a firing pulse repetition rate $f = 10$ Hz. The average thrust was experimentally measured in two ways: (1) indirectly, by fixing the thruster on a thrust stand base, placing the thruster exhaust in front of a lightweight plate mounted on a movable arm of a micro-newton-level torsional thrust stand [Fig. 1(b)], and (2) by calculating the experimental data according to the formula $T = 0.63 m_i v_i f \int_0^{\tau_i} I_i(t)dt/Ze$, where $m_i$, $v_i$ are the single ion mass and their average velocity, $f$ is the pulse repetition rate, $I_i(t)$ is the total ion current waveform with duration $\tau_i$, and $Z = 2$ is the ion mean charge stage. The thrust-to-power ratio TPR was measured by dividing the average thrust $T$ over the total power $P_{\mathrm{tot}}$ which is the sum of average powers dissipated in the first stage $P_{\mathrm{arc}}$, in the second (MPD) stage $P_{\mathrm{MPD}}$, and in the PPU ($P_{\mathrm{PPU}}$),

$$\begin{aligned}\mathrm{TPR} &= T/(P_{\mathrm{arc}} + P_{\mathrm{MPD}} + P_{\mathrm{PPU}}) \\ &= T/f\left(\int_0^{\tau_{\mathrm{arc}}} I_{\mathrm{arc}}(t)U_{\mathrm{arc}}(t)dt + \int_0^{\tau_{\mathrm{MPD}}} I_{\mathrm{MPD}}(t)U_{\mathrm{MPD}}(t)dt \right. \\ &\quad \left. + \int_0^{\tau_{\mathrm{PPU}}} I_{\mathrm{PPU}}(t)U_{\mathrm{PPU}}(t)dt\right), \qquad (1)\end{aligned}$$

where $\tau_{\mathrm{arc}}$, $\tau_{\mathrm{MPD}}$, and $\tau_{\mathrm{PPU}}$ are current pulse durations in the first stage, MPD stage, and in PPU, respectively. Efficiency $\eta$ was estimated by dividing the average power of thruster exhaust over $P_{\mathrm{tot}}$: $\eta = 100\%(T\, v_i/P_{\mathrm{tot}})$.

The results demonstrating the onset of the arc in the second stage, for a thruster with or without a magnetic field, are given in Fig. 2. The absence of a magnetic field results in long powerful pulses in the first stage, and the arc tends to switch to the dc mode [Fig. 2(a)]. Once the magnetic field is added, the first stage produces the plasma in very short and low-power pulses [Fig. 2(b)]. One can see that there is a threshold for "activation" of the second stage—after ∼10 V without a magnetic field [Figs. 2(c) and 3(a)], and ∼30 V with a magnetic field [Figs. 2(d) and 3(a)]. Without the magnetic field, the exhausting total ion current is weakly dependent on the $U_{\mathrm{MPD}}$ stage voltage and more or less constant in time [Fig. 2(e)]; but with a magnetic field, it drastically jumps only after a certain threshold of ∼30 V [Fig. 2(f)].

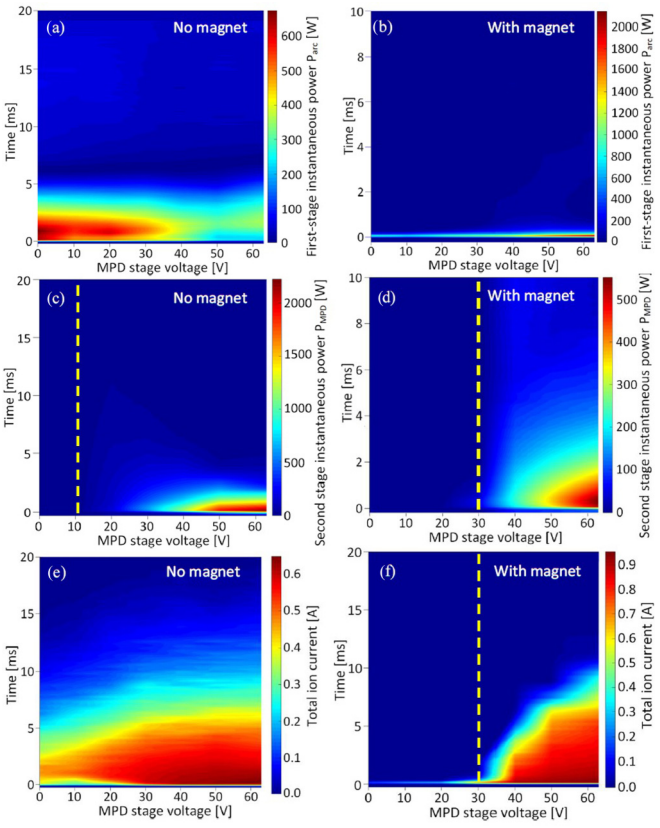


FIG. 2. Instantaneous powers dissipating in the first and the second (MPD) stages, and the total expelling ion current, within the single pulse, for the thruster in "no magnet" and "with magnet" configurations.

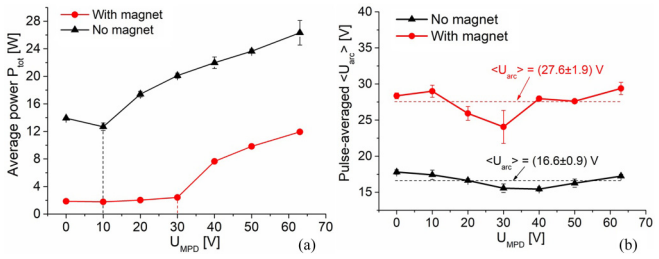


FIG. 3. (a) The onset behavior of vacuum arc in a MPD thruster: Average power dissipated in the MPD stage jumps after a certain threshold of $U_{\mathrm{MPD}}$ voltage of ∼10 V (no magnet) and ∼30 V (with magnet). (b) Pulse-averaged $\langle U_{\mathrm{arc}}\rangle$ vs $U_{\mathrm{MPD}}$ for the with magnet and no magnet cases. Dashed lines represent the average value of $\langle U_{\mathrm{arc}}\rangle$.

Without a magnetic field, the average power, dissipating in the first stage, does not depend on the MPD stage voltage and remains comparable with the power in the second stage. However, with a magnetic field, the first-stage power abruptly drops just to several W, and after a certain $U_{\mathrm{MPD}}$ voltage (∼30 V), the highest power now is dissipating in the MPD stage, but this power with a magnetic field is much less than without a magnetic field [Fig. 3(a)]. These results suggest that the magnetic field positively affects the thruster performance, decreasing the power losses in the first stage, preventing switching into a dc arc, and enhancing the plasma generation and its acceleration in the second stage.

Let us propose a qualitative explanation for such threshold-like behavior. First, let us note that such behavior is observed not only in the "with magnet" case, but also even in the "no magnet" case [Fig. 3(a)]. This fact allows us to suggest that this happens due to an electric field-related effect, and the magnetic field enhances it. One of the most possible factors responsible for the threshold voltage value seems to be related to the first-stage pulse-averaged arc burning voltage,

$$\langle U_{\mathrm{arc}}\rangle = \frac{1}{\tau_{\mathrm{arc}}}\int_0^{\tau_{\mathrm{arc}}} U_{\mathrm{arc}}(t)dt. \tag{2}$$

The dependences of $\langle U_{\mathrm{arc}}\rangle$ on $U_{\mathrm{MPD}}$ for the "with magnet" and "no magnet" cases are given in Fig. 3(b). One can see that pulse-averaged $\langle U_{\mathrm{arc}}\rangle$ weakly depends on $U_{\mathrm{MPD}}$ voltage, but strongly depends on the presence of a magnetic field. Also, we may see that the average values of $\langle U_{\mathrm{arc}}\rangle$ (27.6 and 16.6 V) are very close to the respective threshold voltage values for the with magnet and without magnet cases (∼30 and ∼10 V, respectively).

At the initial moment of the arc ignition (when there is no plasma), the anode-cathode voltage formed by the first-stage PPU has the form of a quite high (with an amplitude of up to several hundreds of V) but very short peak. Once the plasma is ignited, this voltage drops down to the arc burning voltage defined by the cathode material [15] and which can be estimated according to Eq. (2). First-stage plasma acquires a potential close to the potential of the anode (i.e., arc burning voltage), therefore, any voltage on the MPD stage below this plasma potential (i.e., below the pulse-averaged arc burning voltage) will repel electrons from the MPD electrode and therefore the electron current $I_{\mathrm{MPD}}$ toward the MPD electrode will be close to zero. After an increase of $U_{\mathrm{MPD}}$ to values higher than $\langle U_{\mathrm{arc}}\rangle$, the plasma electrons feel the accelerating field from the cathode toward the MPD electrode, and their current $I_{\mathrm{MPD}}$ toward the MPD electrode grows with the $U_{\mathrm{MPD}}$ voltage.

In the case with the presence of a magnetic field, the first-stage plasma electrons are magnetized, and therefore pulse-averaged arc burning voltage is becoming much higher. Therefore, in order to attract electrons toward the MPD electrode, higher $U_{\mathrm{MPD}}$ voltages are required. This obviously leads to higher threshold values.

The assumption made above was supported by measurements of a pulse-averaged plasma potential versus $U_{\mathrm{MPD}}$ in the with magnet and no magnet cases. The experimental setup for this measurement included a ceramic tube with a mounted Langmuir probe tip (a ring with a diameter of 2 mm and length 1 mm). The ring was mounted on the end of the ceramic tube, and placed at and aligned with the axis of the thruster, with the ring directed toward the cathode. The Langmuir probe was movable along the axis in 0.5-mm steps. During the experiment, the position of the probe tip was fixed at around 0.5 mm from the anode. The floating potential was measured by a voltage sensor, connected to the probe tip via a screened BNC cable. The floating potential was measured in the two modes, with and without the magnet, versus the $U_{\mathrm{MPD}}$ voltage (0–63 V), for the other experimental parameters that remained unchanged. The floating potential waveform data were used to directly calculate the pulse-averaged plasma potential $\langle\varphi_p\rangle$ according to the formula

$$\langle\varphi_p\rangle = \langle\varphi_{\mathrm{fl}}\rangle + \ln(m_i/2\pi m_e)kT_e/2e, \tag{3}$$

where $\langle\varphi_{\mathrm{fl}}\rangle$ is the pulse-averaged probe floating potential. Here, the electron temperature $T_e$ was assumed to be independent from the presence of the magnetic field and was taken to be equal to 3.5 eV according to the data from the literature [15] for copper vacuum arc plasma. This assumption is supported by a well-known fact that in the vacuum arc plasma the electron temperature is nearly constant [9,16]. One can see from Fig. 4(a) that the plasma potential significantly changes with $U_{\mathrm{MPD}}$, while $\langle U_{\mathrm{arc}}\rangle$, as follows from Fig. 3(b) above, changes slightly. This is understood since for the fixed electron temperature, the plasma potential will be strongly dependent on the electron loss rate determined by the potential on the neighboring electrodes (mainly on the MPD electrode). However, one can see that the plasma potential is

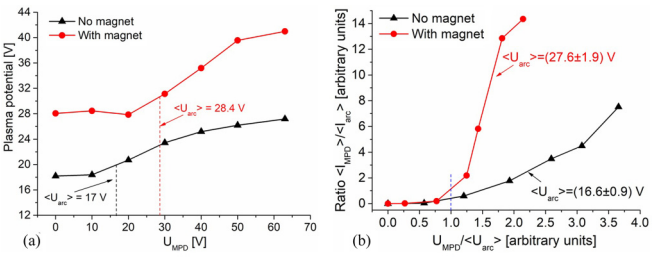


FIG. 4. (a) Pulse-averaged plasma potential with respect to the grounded cathode, vs $U_{\mathrm{MPD}}$, for with magnet and no magnet cases. Dashed lines correspond to the pulse-averaged arc burning voltages. (b) Pulse-averaged $I_{\mathrm{MPD}}/I_{\mathrm{arc}}$ ratio vs $U_{\mathrm{MPD}}/\langle U_{\mathrm{arc}}\rangle$, for with magnet and no magnet cases.

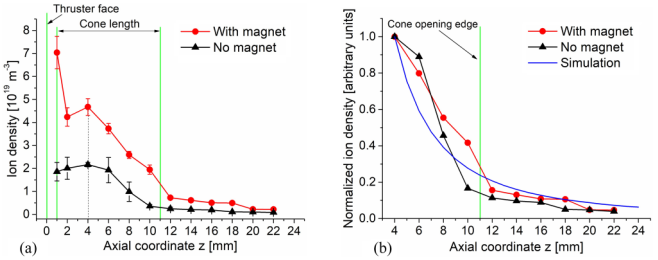


FIG. 5. (a) Pulse-averaged ion density vs axial coordinate, at $U_{\mathrm{MPD}} = 63$ V, for with magnet and no magnet configurations. Axial coordinates for the face of the thruster first stage, and cone boundaries are given by the green solid lines. (b) Normalized (to their maxima at $z = 4$ mm) curves of pulse-averaged ion density vs $z$, for with magnet and no magnet configurations, and simulation (blue line).

connected with the arc burning voltage, since this potential starts growing after $U_{\mathrm{MPD}}$ exceeds $\langle U_{\mathrm{arc}}\rangle$ for the corresponding with magnet or no magnet cases.

Another argument supporting the explanation for an abrupt increase in thruster performance due to the drastic growth in the current to the second MPD stage occurring when $U_{\mathrm{MPD}}$ exceeds the plasma potential, are the ratios of pulse-averaged $\langle I_{\mathrm{MPD}}\rangle/\langle I_{\mathrm{arc}}\rangle$ vs $U_{\mathrm{MPD}}/\langle U_{\mathrm{arc}}\rangle$ given in Fig. 4(b). It is clearly seen that for both cases, there is no $\langle I_{\mathrm{MPD}}\rangle$ current at $U_{\mathrm{MPD}}$ less than $\langle U_{\mathrm{arc}}\rangle$ (i.e., for $U_{\mathrm{MPD}}/\langle U_{\mathrm{arc}}\rangle$ of less than 1), and we see a significant increase in $\langle I_{\mathrm{MPD}}\rangle/\langle I_{\mathrm{arc}}\rangle$ after this value.

Now let us find the region of ion acceleration inside the cone volume. Let us assume that the total flow of ions entering the narrow part of the cone will be the same at the cone exhaust (since the MPD electrode is positive and ions will be reflected from its walls). Therefore, one can write an expression for the ion flow valid for any cross section of the cone and even further,

$$j_{i0}S_0 = j_z S_z, \tag{4}$$

where $j_{i0}$ is the ion current density at the plane of the cone narrow opening having a cross-sectional area $S_0$, and $j_z$ and $S_z$ are the corresponding values at any axial coordinate $z$. Assuming that $v_i(0) = v_i(z)$, we can derive the final expression for the normalized ion density function versus axial coordinate,

$$n_i(z)/n_i(0) = r_0^2/(r_0 + z\tan\alpha)^2. \tag{5}$$

One can expect that if the ions are accelerating with a $z$ coordinate $[v_i(0) \neq v_i(z)]$, the experimentally measured $n_i(z)/n_i(0)$ will go steeper than the calculated according to Eq. (5), and this could help us find the region of ion acceleration. Such an experiment was conducted using the axially movable Langmuir probe described above. The initial axial coordinate ($z = 0$) was adjusted to the cathode surface, and then the probe tip coordinate was varied in steps of 2 mm, from 1 up to 22 mm with respect to the cathode surface. The probe tip was biased with a battery set to $-53$ V with respect to the ground. The ion current waveform was measured as a voltage across a 100-Ω resistor. Since the probe surface was directed perpendicular to the supersonic plasma flow, we used a Bohm formula to calculate a pulse-averaged ion density $\langle n_i\rangle$ from the probe current,

$$\langle n_i\rangle = (\sqrt{m_i}/A_p Ze\sqrt{2kT_e})\langle I_i\rangle, \tag{6}$$

where $A_p$ is the probe surface area, and $\langle I_i\rangle = \frac{1}{\tau_i}\int_0^{\tau_i} I_i(t)dt$ is a pulse-averaged ion current calculated from the ion current waveform measured by the probe tip. The results of the experiments and simulation are given in Fig. 5.

One can see absolute values of the ion density for the with magnet configuration in times higher than for the no magnet. There is a rapid drop of ion density in the few millimeters from the cone opening for the with magnet configuration, which can be probably due to the localization of the ion accelerating region in this area (the region with a high density of magnetic field and with the highest current density flowing from the first stage towards the accelerating cone). However, for the no magnet configuration, there are no drops in ion density; instead of dropping, the ion density slightly grows to some maximum at about $z = 4$ mm, and then goes down [Fig. 5(a)]. After a local maximal point at $z = 4$ mm inside the cone, the ion density curves decay for both configurations [Fig. 5(b)].

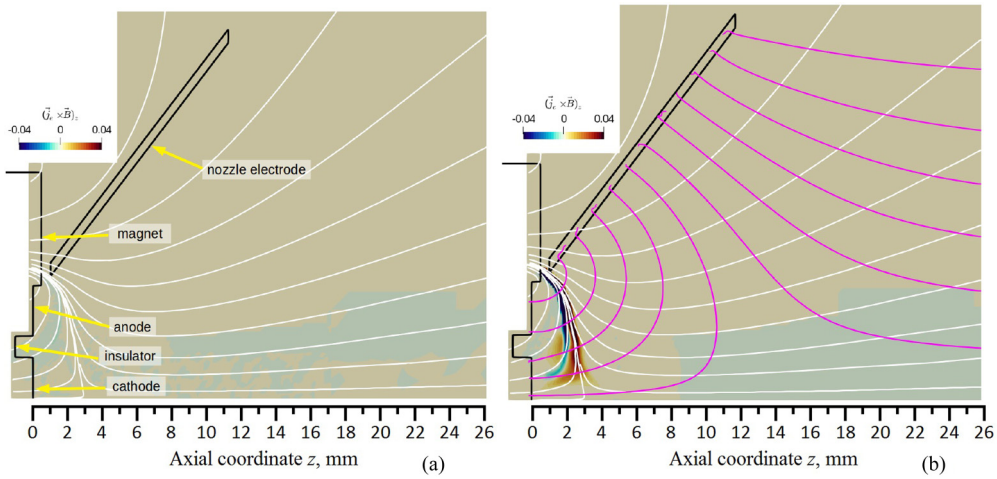


FIG. 6. Normalized axial component of the Lorentz force for (a) $U_{\mathrm{MPD}} = 0$ and (b) $U_{\mathrm{MPD}} = 63$ V. The white lines depict the magnetic field, while the purple lines denote the electric field.

This decay is due to a free expansion of the plasma, and may happen at the constant velocity of ions in this region, as follows from the estimations given above.

The physics of the thrust gain and the threshold behavior of the μCAT-MPD thruster is additionally illustrated using particle-in-cell (PIC) simulations below. These simulations have been performed using the open-source, two-dimensional electrostatic particle-in-cell code STARFISH [17]. The computational domain consisted of a Cartesian mesh with varying resolution and linear splines denoting the thruster. The magnetic field was modeled in FEMM [18] and subsequently imported into the simulation. We introduce electrons and copper ions at random positions within the "beam" by picking random positions within a cylindrical region extending from the cathode to the nozzle exit. Both ions and electrons were sampled from the Maxwellian distribution with $T = 5000$ K and drift velocity $v_z = 50$ km/s. The fully kinetic electrostatic particle-in-cell (ES-PIC) method was then used to advance particle velocities and positions. The simulation was run for 5000, $5 \times 10^{-12}$ s time steps which was a sufficient time to establish a steady state within the electron population. At this time step (5 ps), which was many times shorter than the electron cyclotron period (∼0.18 ns) and the characteristic time of electron-ion collisions (∼1 ns), the electron cyclotron motion is resolved with approximately five steps in the region of peak magnetic field strength, and ten steps in the region of interest. The simulation utilized a mesh composed of multiple domains, with the grid spacing ranging from $1.25 \times 10^{-4}$ m in the vicinity of the thruster to $10^{-3}$ m in the far-field region. Particle velocities were interpolated to the grid to compute mesh-averaged macroscopic stream velocities. Subsequently, the electron current density was computed from $j_e = -en_e\vec{v}_e$, and the Lorentz force was computed by taking a cross product with the magnetic field. The two plots in Fig. 6 compare the impact of the accelerator electrode voltage on this component. With $U_{\mathrm{MPD}} = 0$, we do not observe any noticeable contribution to thrust from the Lorentz force. However, with $U_{\mathrm{MPD}} = 63$ V, there is a clear axial contribution.

From the simulation results given for $U_{\mathrm{MPD}} = 63$ V [Fig. 6(b)] one can see that the region of the maximal values of the $J \times B$ force (at distances between 1 and 3 mm from the cathode surface) agrees well with the experimentally observed region of the acceleration of the ions [Fig. 5(a), with magnet case]. This is an additional argument supporting the claim that it is the $J \times B$ force that causes an increase in thrust.

The discovered onset of the magnetized vacuum arc in a two-staged μCAT-MPD thruster allows one to drastically increase its thrust, TPR, and efficiency, as illustrated in Fig. 7. From Fig. 7 one can see that with the magnetic field, at low

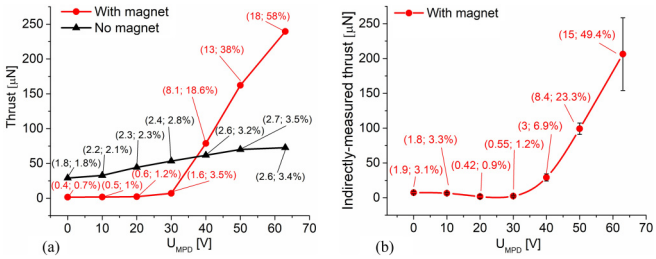


FIG. 7. (a) Thrust, estimated from the electrical measurements of the thruster in with magnet and no magnet configurations, (b) and indirectly measured thrust using the thrust stand in configuration with magnet. The first numbers in brackets mean the thrust-to-power ratio (in μN/W), and the second ones with percent signs mean efficiency, for the respective data points.

$U_{\mathrm{MPD}}$ voltages (0–30 V), the thrust and TPR values (2–10 μN and 0.5–2 μN/W) remain low and comparable with the respective parameters of single-stage μCATs achieved before without any acceleration stages. However, after the $U_{\mathrm{MPD}}$ voltage increase from ∼30 V to its maximal value of 63 V, both thrust and TPR rapidly grow and reach 210 μN and 15 μN/W, respectively, together with a high efficiency of ∼50%. Note that thrust and TPR growth at high $U_{\mathrm{MPD}}$ voltages does not demonstrate any trends to saturation, which looks promising and requires further study. However, one can expect a decrease of efficiency at high levels of power due to the finite size of the cathode surface limiting the MPD current density and leading to a high degree of cathode nonuniform consumption. It should be pointed out that cathode erosion is an essential process since the cathode material is the propellant in such a thruster [19]. A single cathode was shown to be performing around 1 million pulses in optimal geometry [20], or by using special cathode feeding systems [21]. The second stage described in this Rapid Communication leads to a significant improvement of the performance. Note than for the thruster without a magnetic field [Fig. 7(a)], thrust, TPR, and efficiency grow insignificantly with $U_{\mathrm{MPD}}$.

In conclusion, our findings demonstrate the way to improve thrust together with the thrust-to-power ratio and efficiency of low-power MPD thrusters, owing to the onset of a magnetized arc after a certain threshold voltage on the second MPD stage.

The work was supported by an Air Force Office of Scientific Research, FA9550-19-1-0166 (Dr. Mitat Birkan is program manager), NASA DC Space Grant Consortium, and the National Science Foundation Grant No. 1747760.

[1] R. M. Myers, M. A. Mantenieks, and M. R. LaPointe, in *Conference on Advanced SEI Techonologies*, AIAA Paper 91-3568 (AIAA, Reston, VA, 1991).

[2] M. Zuin, R. Cavazzana, E. Martines, G. Serianni, V. Antoni, M. Bagatin, M. Andrenucci, F. Paganucci, and P. Rossetti, Phys. Rev. Lett. **92**, 225003 (2004).

[3] A. I. Smolyakov, W. Frias, I. D. Kaganovich, and Y. Raitses, Phys. Rev. Lett. **111**, 115002 (2013.

[4] J. S. Sovey and M. A. Mantenieks, J. Propul. Power **7**, 71 (1991).

[5] E. Hand, Science **348**, 176 (2015).

[6] S. Asmar and S. Matousek, in *SpaceOps 2016 Conference*, AIAA Paper 2016-2483 (AIAA, Reston, VA, 2016).

[7] I. Levchenko, M. Keidar, J. Cantrell, Y.-L. Wu, H. Kuninaka, K. Bazaka, and S. Xu, Nature (London) **562**, 185 (2018).
[8] I. Levchenko, S. Xu, G. Teel, D. Mariotti, M. L. R. Walker, and M. Keidar, Nat. Commun. **9**, 879 (2018).
[9] M. Keidar, I. Beilis, R. L. Boxman, and S. Goldsmith, J. Phys. D: Appl. Phys. **29**, 1973 (1996).
[10] R. L. Boxman, D. M. Sanders, and P. J. Martin, *Handbook of Vacuum Arc Science and Technology*, 1st ed. (Noyes, Park Ridge, NJ, 1996).
[11] A. S. Gilmour Jr. and D. L. Lockwood, Proc. IEEE **60**, 977 (1972).
[12] A. S. Gilmour Jr., J. R. Graham, D. L. Lockwood, R. J. Clark Jr., and H. Veron, in *AIAA 4th Propulsion Joint Specialist Conference* (AIAA, Reston, VA, 1968).
[13] R. Dethlefsen, AIAA J. **6**, 1197 (1968).
[14] O. Jarrett, Jr., J. M. Hoell, Jr., and D. L. Lockwood, in *AIAA 8th Electric Propulsion Conference*, AIM Paper 70-1146 (AIAA, Reston, VA, 1970).
[15] A. Anders, B. Yotsombat, and R. Binder, J. Appl. Phys. **89**, 7764 (2001).
[16] M. Keidar, I. I. Beilis, and I. G. Brown, J. Appl. Phys. **84**, 5956 (1998).
[17] https://www.particleincell.com/starfish/.
[18] http://www.femm.info/wiki/HomePage.
[19] J. Kolbeck, A. Anders, I. I. Beilis, and M. Keidar, J. Appl. Phys. **125**, 220902 (2019).
[20] D. B. Zolotukhin and M. Keidar, Plasma Sources Sci. Technol. **27**, 074001 (2018).
[21] I. Kronhaus, M. Laterza, and Y. Maor, Rev. Sci. Instrum. **88**, 043505 (2017).